Review Article

Nano Research
2021, 14(6): 1878–1888

ISSN 1998-0124 CN 11-5974/O4
https://doi.org/10.1007/s12274-020-3001-8

Avalanche photodetectors based on two-dimensional layered materials

Jinshui Miao[1] (✉) and Chuan Wang[2] (✉)

[1] *State Key Laboratory of Infrared Physics, Shanghai Institute of Technical Physics, Chinese Academy of Sciences, Shanghai 200083, China*
[2] *Department of Electrical and Systems Engineering, Washington University in St. Louis, St. Louis, Missouri 63130, USA*

© Tsinghua University Press and Springer-Verlag GmbH Germany, part of Springer Nature 2020
Received: 13 May 2020 / **Revised:** 19 July 2020 / **Accepted:** 20 July 2020

ABSTRACT

The past decade has witnessed a dramatic increase in interest in emerging photodetectors built from two-dimensional (2D) layered materials. A major driver of this trend is the growing demands for lightweight, uncooled, and even flexible photodetection technology. However, 2D layered materials always suffer from low light absorption coefficients due to their atomically thin nature. Impact ionization, which can achieve carrier multiplication, is a promising strategy to design 2D photodetectors with high detection efficiency. In this review, typical types of photodetection mechanisms in 2D photodetectors are first summarized. We then discuss the avalanche mechanism induced by impact ionization and avalanche photodetectors based on conventional silicon and III-V compound semiconductors. Finally, a host of emerging avalanche photodetectors based on 2D materials and their van der Waals heterostructures, and their potential applications in the field of photon-counting technologies are detailed. By reviewing the recent progress and discussing challenges faced by 2D avalanche photodetectors, this review aims to provide perspectives on future research directions of 2D material-based ultrasensitive photodetectors such as single-photon detectors.

KEYWORDS

two-dimensional materials, van der Waals heterostructures, photodetectors, impact ionization, avalanche photodiodes, single-photon detectors

1 Introduction

Photodetectors are one of the most ubiquitous types of technology in use today [1]. They have been widely used for various purposes, such as sensors that can automatically open the doors, receivers for infrared signal from remote controllers, photodiodes in a fiberoptic connection, image sensors in the cell phones or cameras, and focal plane arrays used for space exploration. Photodetectors built from conventional bulk semiconductors such as silicon, InGaAs, InSb, HgCdTe, etc. can detect the photons with wavelength ranging from visible to far-infrared [2–5]. In the past few decades, the material growth and device fabrication technologies are becoming mature, which enable much more sophisticated photodetectors with high detectivity, fast response and high resolution. However, lightweight, uncooled, and even mechanically flexible photodetectors are now highly appealing in the emerging field of wearable electronics, intelligent robotics, and unmanned aerial vehicle (UAV) or self-driving cars, etc. [6, 7]. To this end, two-dimensional (2D) layered materials with exceptional optical, electrical, and even mechanical properties, have recently received tremendous research interest from photodetector community [8–10]. Compared to conventional bulk materials, 2D layered materials have many unique properties, such as self-passivated surfaces, strong light–matter coupling, gate-tunable Fermi level and mechanical flexibility, etc. [11, 12].

2D layered graphene, being gapless, can interact with light with wavelength ranging from ultraviolet to microwave, thus making it a promising candidate for various types of photodetection applications over a wide spectral range [9, 13–18]. However, its gapless nature prevents the realization of photodetectors with high signal-to-noise ratio [19]. In contrast, 2D transition metal dichalcogenides (TMDs) such as WSe_2 and MoS_2 have thickness-dependent bandgap, exhibiting promising photodetection properties primarily in the visible to near-infrared range [20–22]. Other than graphene and TMDs, 2D black phosphorus (BP) with a direct bandgap ranging from 0.3 eV (bulk form) to 2.0 eV (monolayer form), has also been studied as a potential material candidate for infrared photodetection technology [23–30]. The wide range of material choices, together with van der Waals heterostructures formed by combination of 2D layered materials with other nD-materials (n = 0, 1, and 3), allows for realization of a variety of photodetectors [19, 31–35].

2D photodetectors with different working mechanisms such as photoconductive [36], photovoltaic [25], and photothermoelectric [37] effects have already been widely studied and well summarized in the literatures. However, avalanche effect via impact ionization in 2D photodetectors has not yet been studied as extensively [38]. Therefore, in this review, we aim to provide a focused discussion on avalanche photodetectors built from 2D layered materials and their van der Waals heterostructures, with an emphasis on their potential applications in the field of single-photon counting technologies.

2 Mechanisms of 2D photodetectors

In this section, we will discuss several working mechanisms of 2D material-based photodetectors. The photodetection

Address correspondence to Jinshui Miao, jsmiao@mail.sitp.ac.cn; Chuan Wang, chuanwang@wustl.edu

mechanisms include photoconductive, photovoltaic, photo-thermoelectric, photo-bolometric and photogating effects [39–43]. The photocurrent generation in some 2D photodetectors may also arise from several mechanisms combined [44, 45].

In 2013, O. Lopez-Sanchez et al. reported monolayer MoS_2 photodetectors based on photoconductive effect, as shown in Fig. 1(a) [43]. In the OFF state ($V_g < V_t$; V_g represents gate voltage, V_t represents threshold voltage), the incident photons can generate electron-hole pairs in MoS_2, which will be swept to the electrodes by applying a drain-source bias (V_{ds}). The photocurrent increases linearly with increasing V_{ds} due to the shortened carrier transit time. In the ON state ($V_g > V_t$), the Schottky barrier at the metal/MoS_2 junction is significantly reduced, so that the thermionic and tunneling currents also contribute to the channel current in addition to photocurrent. When the device is operated in the ON state, it suffers from large background noise. 2D van der Waals heterojunction photodetectors are typically dominated by photovoltaic effect, as illustrated in Fig. 1(b) [42]. Photovoltaic effect refers to the phenomenon that photo-generated carriers get separated by internal electric field in heterojunction, homojunction or Schottky junction. In WSe_2/MoS_2 p-n junction, photons are absorbed in the WSe_2 and MoS_2, generating electron–hole pairs in each layer. And then the electrons and holes are spatially separated across the p-n junction via built-in field. The relaxed carriers then diffuse laterally to the source and drain contacts leading to photocurrent. During carrier diffusion, interlayer recombination may occur, which reduces the efficiency of the 2D photodetectors. In some 2D photodetectors, photovoltaic and photoconductive effects both show high gain, as illustrated in Fig. 1(c) [45]. In this type of 2D MoS_2 device, the photovoltaic effect results in a shift in the transistor threshold voltage because the charges transfer from the channel to the nearby molecules, such as SiO_2 surface-bound H_2O molecules. And the photoconductive effect is attributed to the trapping of carriers in band tail states of 2D MoS_2. In 2016, Q. Guo et al. reported 2D BP mid-infrared photodetectors and there were two distinct mechanisms (photovoltaic and photogating) accounting for the photocurrent generation, as illustrated in Fig. 1(d) [39]. The photogating effect means that the photo-generated carriers are trapped in the localized states acting as the local gate, which can effectively modulate the device threshold voltage (V_{th}). The photogating effect induced photocurrent (I_{ph}) is related to transconductance (g_m) and threshold shift (ΔV_{th}), that is $I_{ph} = g_m \times \Delta V_{th}$. The other two mechanisms are related to thermal effect, as indicated in Figs. 1(e) and 1(f) [40, 41]. In 2D MoS_2 photodetectors, the gold electrodes and monolayer MoS_2 have different Seebeck coefficients. The local absorption of the laser can create a local heating of the junction between MoS_2 channel and gold electrode [40]. The heating difference is translated into a voltage difference (ΔV_{PTE}) via Seebeck effect, which will drive current through the device. Another thermal-related photo-detection mechanism is photothermally-induced bolometric effect, as shown in Fig. 1(f) [41]. The 2D BP-based flexible photodetectors are fabricated on freestanding polyimide film, in which the thermal conductivity is around 0.2 W/(m·K) [46]. The thermal conductivity of polyimide is significantly lower than that of silicon whose thermal conductivity is around 150 W/(m·K) [47]. The incident laser would create a localized heating spot underneath the 2D BP device, so that the carrier mobility decreases because of enhanced phonon scattering, and consequently leads to negative photocurrent.

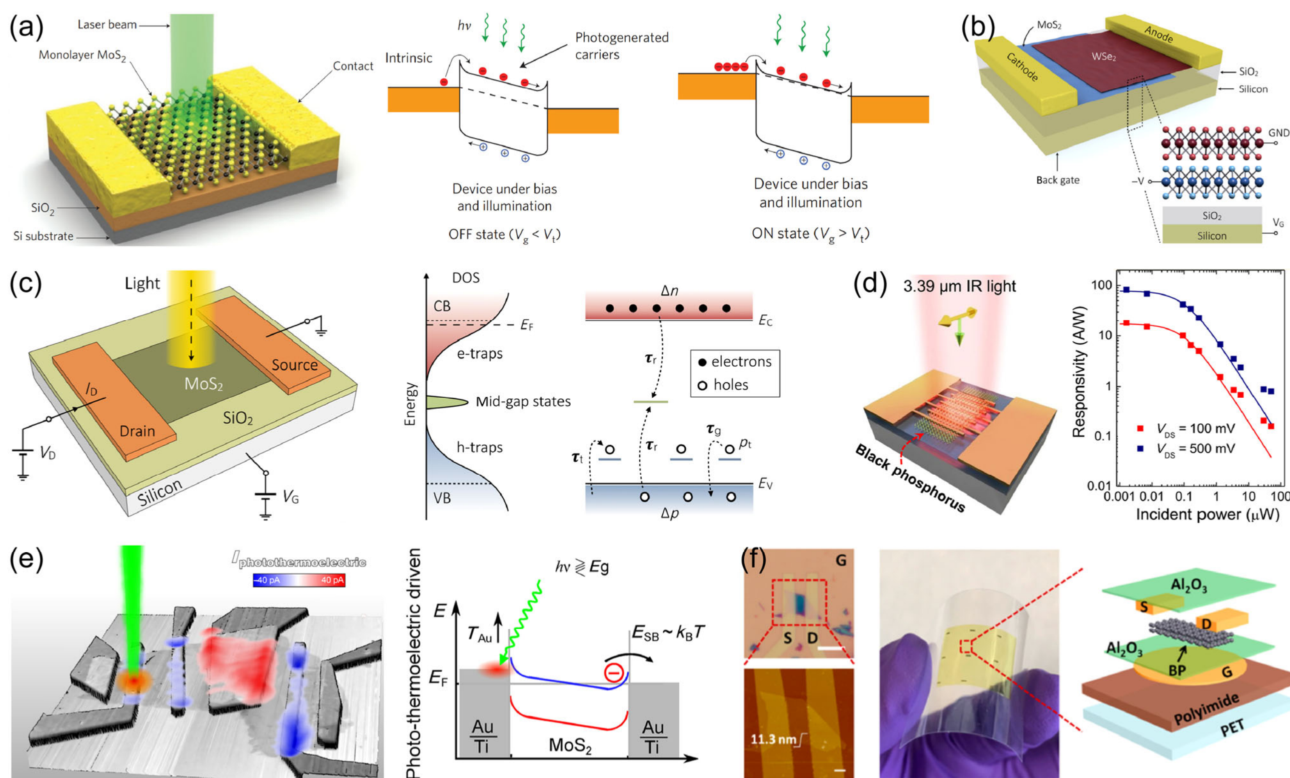

Figure 1 Working mechanisms of photodetectors based on two-dimensional layered materials. (a) Photoconductive effect in monolayer MoS_2 photodetectors (reproduced with permission from Ref. [43], © Macmillan Publishers Limited 2013). (b) Photovoltaic effect in WSe_2/MoS_2 p-n hetero-junction photodetectors (reproduced with permission from Ref. [42], © American Chemical Society 2014). (c) Photoconductive and photovoltaic effect in monolayer MoS_2 photodetectors (reproduced with permission from Ref. [45], © American Chemical Society 2014). (d) Photovoltaic and photogating effect in few-layer BP mid-infrared photodetectors (reproduced with permission from Ref. [39], © American Chemical Society 2016). (e) Photo-thermoelectric effect in monolayer MoS_2 photodetectors (reproduced with permission from Ref. [40], © American Chemical Society 2013). (f) Photo-bolometric effect in few-layer BP photodetectors on flexible substrate (reproduced with permission from Ref. [41], © American Chemical Society 2017).

In addition to these five photodetection mechanisms mentioned above, avalanche photodetection via impact ionization which can achieve carrier multiplication, is also an extremely important mechanism for photodetection applications especially for single-photon counting technologies [48, 49]. The avalanche effect is a special case of the photovoltaic effect. In avalanche photodetectors, the photogenerated carriers are accelerated to an extremely high velocity by strong reverse-biased electric field so that the carriers can gain enough energy to initiate avalanche via impact ionization and more carriers are then generated [50]. In this review, we will first discuss the working principle of such avalanche process, and then single-photon avalanche photodetectors from conventional silicon and III-V compound semiconductors, and finally avalanche photodetectors from emerging 2D materials.

3 Mechanisms of avalanche photodiodes

An avalanche photodiode is an extremely sensitive photodetector which can convert light into current or voltage signal [48]. It can be regarded as the semiconductor analog of the photomultiplier. The avalanche photodiode is typically operated with a relatively high reverse bias voltage of tens or even hundreds of volts [51]. In this regime, the photo-generated electron–hole pairs are accelerated by the electric field, so that they can generate more carriers by impact ionization. The avalanche process occurs within only a few micrometers and can effectively amplifies the photocurrent by a significant factor. Therefore, the avalanche photodiodes can be used as extremely sensitive detectors, which need less electronic amplification.

Figure 2 shows the working principle of silicon-based avalanche photodiodes under the reverse bias condition [52, 53]. The diode is reverse biased to increase the fields in the depletion regions. Figure 2(b) shows the net space charge distribution across the diode due to exposed dopant ions. Under zero bias,

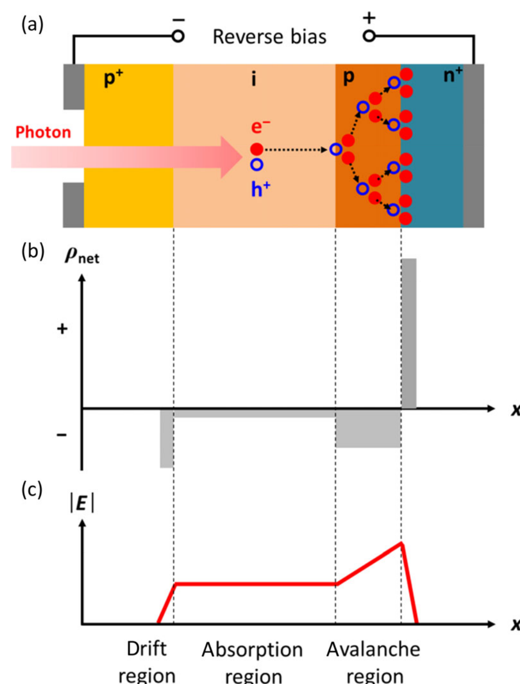

Figure 2 Working mechanisms of avalanche photodiodes. (a) A simplified schematic diagram of a reach-through avalanche photodiode. The structure mainly consists of three regions which are drift region (p^+-silicon), absorption region (i-silicon) and avalanche region (p-n^+-silicon junction). (b) The net space charge density across the photodiodes. (c) Under reverse bias condition, these three regions show different electric field strength and the avalanche region shows the strongest electric field.

the depletion layer in the p-region does not normally extend across this layer to the intrinsic silicon region. But when a sufficient reverse bias is applied, the depletion region in the p-silicon widens to reach-through to the intrinsic silicon region. The field extends from the exposed positively charged donors in the thin depletion region in n^+ layer, all the way to the exposed negatively charged acceptors in the thin depletion region in p^+ side. The electric field is given by the integration of the net space charge density across the diode subject to an applied reverse bias across the device. Figure 2(c) shows the variation in the field across the diode. The field line starts at positive ions and ends at negative ions existing through p, i, and p^+ regions. So, the $|E|$ is maximum at the n^+p junction, then decreases slowly through the p-layer and through the i-layer it decreases slightly as the net space charge density here is small. Finally, the field vanishes at the end of the narrow depletion layer in the p^+ side. An incident photon can generate an electron–hole pair in the absorption region, then the electron drifts to the avalanche region (p-n^+ junction) and the hole drifts to the drift region (p^+ silicon). In the avalanche region, the reverse-biased electric field is strong enough to accelerate the photo-generated electrons to sufficiently high energy to initiate avalanche via impact ionization, generating more carriers. Silicon based avalanche photodiodes are sensitive in the visible to near-infrared wavelength region from 450 to 1,100 nm, with peak response at 600–800 nm [54]. The carrier multiplication factor of the silicon avalanche photodiodes varies between 50 and 1,000 [54]. To detect longer wavelengths up to 1.5 μm, avalanche photodiodes based on III-V compound or germanium semiconductors are good candidates [55–59]. The InGaAs-based avalanche photodiodes are more expensive than germanium-based ones but exhibit much lower noise and higher detection bandwidth [60]. Furthermore, the InGaAs semiconductor has much higher absorption coefficient which allows the use of a rather thin absorption layer.

When the avalanche photodiodes are operated in the Geiger mode with external quenching electronics, they can be used even for single-photon counting technologies [49, 50, 61]. The silicon based single-photon avalanche detectors (SPADs) have exceptional low dark count rate (the probability of recording false counts) below 1 kHz and high detection efficiency (the overall probability of registering a count if a photon arrives at the SPAD) greater than 50% [50]. Geiger mode means that the SPAD is operated above the breakdown voltage, where a photo-generated electron–hole pair can trigger a significant self-sustaining avalanche via impact ionization [61, 62]. In actual application, an external quenching electronics must be used to reset the bias voltage below the breakdown threshold for a short time, so that the avalanche process can be stopped and the SPAD can be used for detection of another incident photon. This process is called dead time which will limit device count rate as not every incident photon can trigger an avalanche process.

4 Avalanche photodiodes built from conventional semiconductors

In principle, any semiconductor material can be used as a multiplication region. Silicon semiconductor can detect photons in the visible to near-infrared wavelength range, with low multiplication noise. Germanium can detect infrared photons out to a wavelength of 1.7 μm but has high multiplication noise. InGaAs can detect out to longer than 1.6 μm and has less multiplication noise than germanium and is normally used as the absorption region of a heterostructure diode, most

typically involving InP as a substrate and as a multiplication layer. HgCdTe-based diodes operate in the infrared up to about 14 μm but require cooling to reduce dark currents. However, semiconductor materials with lower ionization energy and higher carrier mobilities are more suitable for avalanche photodiodes. The most used bulk semiconductors for avalanche photodiodes are silicon and III-V compound semiconductors [54, 55, 62]. This section mainly reviews the operating principle, performance, advantages, and disadvantages of these two types of devices.

4.1 Silicon-based single-photon avalanche photodiodes

In 1963, R. H. Haitz et al. first demonstrated the impact ionization effect in silicon avalanche photodiodes, and then developed one of the first silicon avalanche photodiodes operated in the Geiger mode [63, 64]. The SPADs built from bulk silicon semiconductor show high quantum efficiency (> 50%) because of the thick photon absorption layer (30–50 μm) [54]. However, the thick absorption layer limits its frequency response because the photo-generated carriers in the neutral layer have long diffusion tails, thus limits silicon SPAD's timing resolution to 100 ps level. Therefore, for time-correlated photon-counting technologies, thinner silicon (1–10 μm) needs to be used to improve the timing resolution to sub-20 ps. Moreover, thinner silicon also enables low-bias operation of the SPADs. However, there is a trade-off between thick-junction and thin-junction SPADs. The thick-junction SPADs typically have high detection efficiency but poor timing jitter (the variation in the time interval between the absorption of a photon and the generation of an output electrical pulse from the SPAD), while the thin-junction SPADs have low detection efficiency but good timing jitter [50]. To maintain good timing jitter and improve detection efficiency, K. Zang et al. integrated light-trapping nanostructures with thin-junction SPADs [65]. The basic device structure is shown in Fig. 3(a). In this device structure, silicon epitaxial layers with a total thickness of 2.5 μm are grown on a silicon-on-insulator substrate. The nanostructures on top of the device is etched as an inverse pyramid, with 850 nm period in a square lattice pattern. By exploiting the nanostructures, the quantum efficiency of silicon SPADs was improved by 250% in the near-infrared range, while the timing jitter remains as low as 25 ps.

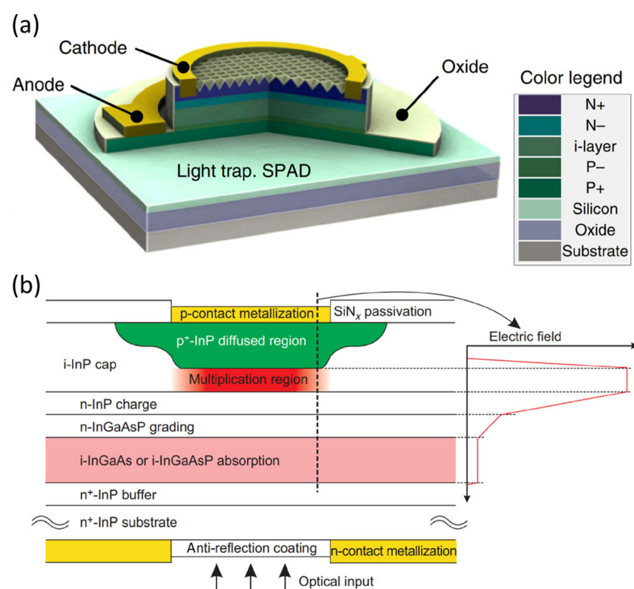

Figure 3 Conventional SPADs based on silicon and InGaAs/InP semiconductors. (a) A 3D cross-sectional schematic of silicon based SPAD with light-trapping nanostructures (reproduced with permission from Ref. [65], © Zang, K. et al. Nature Publishing Group 2017). (b) Cross-sectional schematic of an InGaAs/InP SPAD (reproduced with permission from Ref. [55], © CIOMP 2015).

4.2 III-V semiconductor-based single-photon avalanche photodiodes

The silicon based SPADs can only detect photons with wavelengths of up to around 1,100 nm because the bandgap of silicon semiconductor is 1.1 eV. To extend the detection wavelength to telecommunication range, narrow-bandgap semiconductors must be used [59, 62, 66, 67]. III-V semiconductors such as InGaAs have bandgap of around 0.7 eV, which are promising material candidates for infrared single-photon detection [55]. Figure 3(b) shows a representative device structure of an InGaAs/InP based SPAD which consists of p^+-InP/i-InP multiplication region, n^+-InP charge region, i-InGaAsP grading region, i-InGaAs absorption region, n^+-InP buffer layer, and n^+-InP substrate [55, 68]. Here, the bandgap of i-InGaAs is around 0.7 eV acting as the photon absorption layer. The bandgap of InP is around 1.4 eV, and the p^+-InP/i-InP homojunction is used as carrier multiplication region. All the InGaAs/InP SPADs are based on a separate absorption, charge, and multiplication (SACM) region structure [69]. The multiplication region maintains high electric field to initiate avalanche gain, while the absorption region maintains sufficiently low electric field to minimize field-induced leakage currents. The device is typically operated at the temperature range of 150 to 220 K with dark count rate as low as 3 kHz, detection efficiency as high as 45% across the 1 to 1.6 μm wavelength range, and timing jitter as low as 30 ps [55].

The working mechanism is as follows [69]. When an infrared photon is absorbed by the i-InGaAs layer, an electron–hole pair is generated. The photo-generated electron drifts to the n^+-InP region via electric field and is eventually collected by cathode electrode, while the photo-generated hole drifts to the p^+-InP/i-InP multiplication region. The electric field in the p^+-InP/i-InP region is extremely strong which can accelerate the hole to an exceedingly high velocity to allow it to gain enough energy to initiate avalanche process and to generate more carriers. In the InGaAs/InP SPADs, the n-InGaAsP grading layer is used to avoid carrier accumulation at the InGaAs/InP interface, while the n^+-InP charge layer is designed to provide high electric field in the i-InP multiplication region and low electric field in the i-InGaAs absorption region. In the next section, we will briefly discuss avalanche photodiodes based on conventional semiconductors in nanoscale forms such as 1D silicon or III-V semiconductor nanowires.

4.3 1D semiconductor nanowire-based avalanche photodetectors

Detection with nanoscale photoconductive or photovoltaic devices has relatively poor sensitivity, thus large amplification is required to detect weak light and ultimately a single photon. In 2006, O. Hayden et al. reported avalanche multiplication of the photocurrent in nanoscale p-n heterojunction photodiodes based on crossed Si-CdS nanowires, as shown in Fig. 4(a) [70]. The 1D nanowire avalanche photodiodes have an ultrahigh sensitivity with detection limits of less than 100 photons, and reproducible high multiplication factor of up to 7×10^4. Furthermore, 1D semiconductor nanowires offer unique possibility of combining optical quantum dots with avalanche diodes, thus enabling the conversion of a single photon into a macroscopic current for efficient electrical detection, as shown in Fig. 4(b). G. Bulgarini et al. have demonstrated multiplication of carriers from only a single exciton generated in InAsP

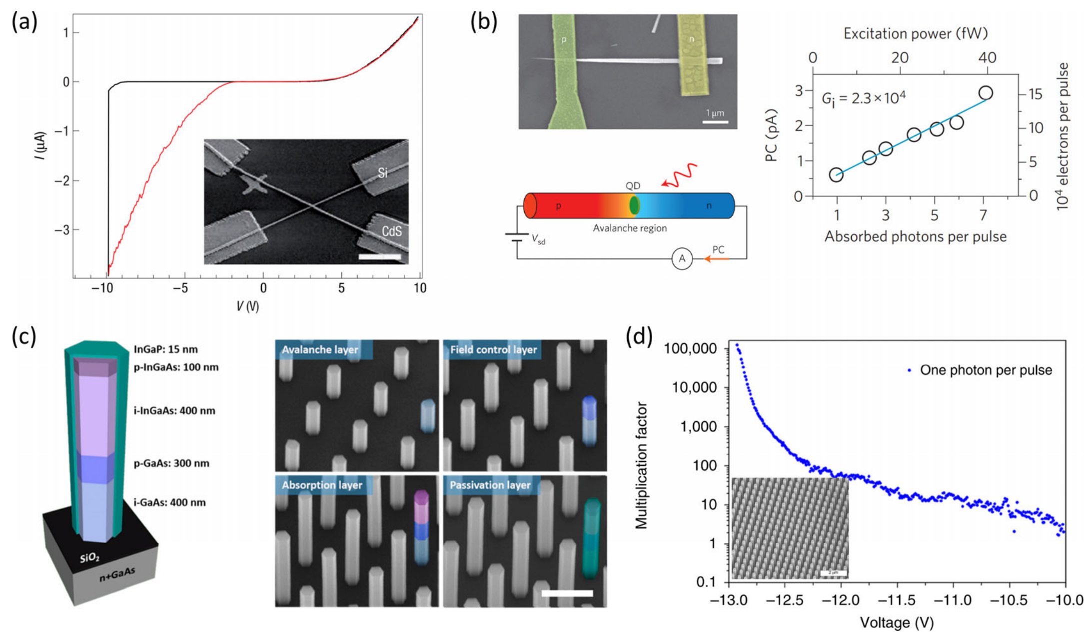

Figure 4 1D nanowire avalanche photodiodes for extremely sensitive photon detection. (a) *I–V* characteristics of n-CdS/p-Si heterojunction avalanche photodiodes in dark (black line) and illuminated (red line) conditions. The device was illuminated with 488-nm light. The inset shows the device scanning electron microscopy (SEM) image. Scale bar, 4 μm. Reproduced with permission from Ref. [70], © Nature Publishing Group 2006. (b) 1D nanowire avalanche photodiode with a single quantum dot located within the nanowire depletion region. The nanowire photodiode response in the avalanche operation shows a high multiplication gain of 2.3×10^4 for one absorbed photon per excitation pulse. Scale bar, 1 μm. Reproduced with permission from Ref. [71], © Macmillan Publishers Limited 2012. (c) InGaAs/GaAs heterojunction nanowire avalanche photodiodes for single-photon detection. The device is composed of InGaAs absorption layer, GaAs avalanche layer, and InGaP passivation shell. Scale bar, 500 nm. Reproduced with permission from Ref. [72], © American Chemical Society 2018. (d) InP nanowire arrays for efficient broadband high-speed single-photon avalanche photodiodes at room temperature. The calculated multiplication gain as a function of applied voltage under illumination of one photon per excitation pulse. The inset shows a SEM image of InP nanowire array after etching, imaged at a tilt angle of 30° from the substrate normal. Scale bar, 2 μm. Reproduced with permission from Ref. [73], © Gibson, S. J. et al., under exclusive license to Springer Nature Limited 2019.

quantum dot after tunneling into a 1D InP nanowire avalanche diode [71]. They significantly reduced the number of excitation events required to electrically detect a single exciton generated in a quantum dot because of the large avalanche amplification of both electrons and holes. In addition, 1D nanowire avalanche photodiodes can also be used for single-photon detection. In 2019, A. C. Farrell et al. reported a new separate absorption and multiplication avalanche photodiode platform consisting of InGaAs/GaAs heterojunction nanowire arrays for single-photon detection, as shown in Fig. 4(c) [72]. The avalanche photodiode consists of 4,400 nanowires and each avalanche event is confined in a single nanowire, which drastically enhances avalanche volume and the number of filled traps. The InGaAs/GaAs nanowire avalanche photodiodes exhibit a low dark count rate of ~ 10 Hz, photon count rates of 7.8 MHz, and timing jitter of less than 113 ps. However, cryogenic operation in the InGaAs/GaAs nanowire avalanche photodiodes limits their widespread applicability. To this end, S. J. Gibson et al. present an approach using tapered InP nanowire p-n junction arrays for efficient broadband high-speed single-photon detection at room temperature, as illustrated in Fig. 4(d) [73]. The truncated conical nanowire structure enables a broadband photoresponse with external quantum efficiency exceeding 85%, high gain beyond 10^5, and excellent timing jitter below 20 ps. Such nanoscale avalanche photodetectors based on 1D quantum nanowires open new possibilities for applications in quantum communications, remote sensing, and dose monitoring for cancer treatment, etc.

5 Avalanche photodetectors built from 2D layered materials

Atomically thin 2D materials have attracted tremendous research interest from photodetector community due to their exceptional optoelectronic properties. However, 2D material-based photodetectors always suffer from low light absorption coefficients, limiting their practical applications [74, 75]. To achieve high gain in 2D photodetectors, impact ionization, which supports photo-generated carrier multiplication, can be used. Furthermore, 2D materials can potentially initiate the impact ionization of avalanche breakdown with relatively low applied bias in a short active region (< 10 nm) because of their atomically thin nature, leading to carrier multiplication with a high gain, low bias, and superior noise performance. Further, 2D materials can easily achieve ballistic avalanche with low avalanche noise due to the nanoscale active region. In this section, we will discuss 2D materials and their van der Waals heterostructures for applications in avalanche photodetectors. In principle, all 2D semiconductors can be used for multiplication region, while those with lower ionization energies and higher carrier mobilities are more suitable for avalanche devices. Table 1 summarizes performance metrics of various types of photodetectors based on 2D materials and their van der Waals heterojunctions including InSe, BP, BP/InSe, MoS_2/Si, MoS_2, BP/MoS_2 [20, 30, 33, 38, 76–80]. It is worth noting that the external quantum efficiency of all 2D avalanche photodetectors exceeds 100% which is attributed to impact-ionized carrier multiplication. However, the external quantum efficiency of these 2D photodetectors is less than unity, because not all the incident photons are absorbed to create free electron–hole pairs that can be collected and give rise a photocurrent, and no impact-ionized carrier multiplication occurs in 2D photodetector devices. However, most 2D avalanche photodetectors reported so far still need large bias to initiate impact ionization because of large Schottky barrier between 2D channel and metal contacts. Using 2D van der Waals heterojunctions

Table 1 Performance metrics of varions 2D photodetectors

Detector type	External quantum efficiency	Gain	Responsivity	Wavelength	Operation temperature
InSe avalanche photodetectors [76]	11.1	152	4.86 A/W	543 nm	295 K
BP avalanche photodetectors [78]	2.719	272	1.16 A/W	532 nm	295 K
BP avalanche photodetectors [77]	4.77	7	2 A/W	520 nm	295 K
BP/InSe avalanche phododiodes [38]	24.8	10^4	80 A/W	4 μm	10–180 K
MoS_2/Si avalanche photodiodes [79]	4.31	10^3	2.2 A/W	633 nm	295 K
InSe photodetectors [80]	0.44	—	244 mA/W	685 nm	295 K
BP photodetectros [30]	0.0093	—	4.8 mA/W	640 nm	295 K
MoS_2 photodetectros [20]	0.017	—	7.5 mA/W	450–800 nm	295 K
BP/MoS_2 photodiodes [33]	0.35	—	0.9 A/W	2.5–3.5 μm	295 K

instead of metal/semiconductor Schottky junctions can reduce the breakdown voltage in 2D avalanche photodetectors. In 2019, A. Gao et al. reported vertical BP/InSe ballistic avalanche photodiodes to significantly reduce applied voltage, but the devices must be operated in low temperature condition. Therefore, further improvements for 2D avalanche photodetectors with low bias, high gain, and room-temperature operation are needed in the future.

5.1 2D InSe avalanche photodetectors

S. Lei et al. reported the use of avalanche effect in 2D InSe field-effect transistors to enhance the photoresponse [76]. In their study, large Schottky barrier in the aluminum/2D InSe contact was exploited to enable large bias voltages of more than 50 V. The 2D InSe avalanche photodetectors have been demonstrated to have an external quantum efficiency of up to 866% and fast response time of 87 μs. The working principle of 2D InSe avalanche photodetectors is shown in Fig. 5(a). When the bias voltage is less than 12 V, the electric field is not strong enough to accelerate the photo-generated electron–hole pairs. The 2D InSe device is operated as a normal photoconductive device and the externally applied electric field just separates the electron–hole pairs and sweeps them into external electrodes (Fig. 5(a)(i)). When the bias voltage is between 12 to 50 V, the photo-generated electron–hole pairs can gain enough energy from the strong electric field to initiate avalanche by impact ionization and more charge carriers can be generated by avalanche. Therefore, the device photocurrent exhibits an abrupt increase with large bias voltage (Fig. 5(a)(ii)). However, with further increased bias voltage (> 50 V), the Schottky barrier at the metal/semiconductor junction undergoes breakdown process, where both photocurrent and dark current increase dramatically leading to low signal-to-noise ratio (Fig. 5(a)(iii)). The best operation voltage is between 30 to 50 V.

Figures 5(b) and 5(c) show the photocurrent response as a function of incident laser wavelength and bias voltage. The peak response is at ~ 510 nm and dark current remains low even the bias is below 50 V because the large Schottky barrier effectively suppresses the noise carrier injections. However, when the bias voltage exceeds 50 V, the dark current exhibits an abrupt increase, which is attributed to the reverse-biased breakdown process at the Schottky junction region. The quantum efficiency can be as high as 1,110% with avalanche gain of 152 when the device is operated with a bias voltage of greater than 50 V but the device would suffer from high noise level as demonstrated in Fig. 5(d) that the photocurrent starts to deviate from linear increase trend at 50 V. Finally, the time-resolved photocurrent response presents a decay time of 60 μs (Fig. 5(e)).

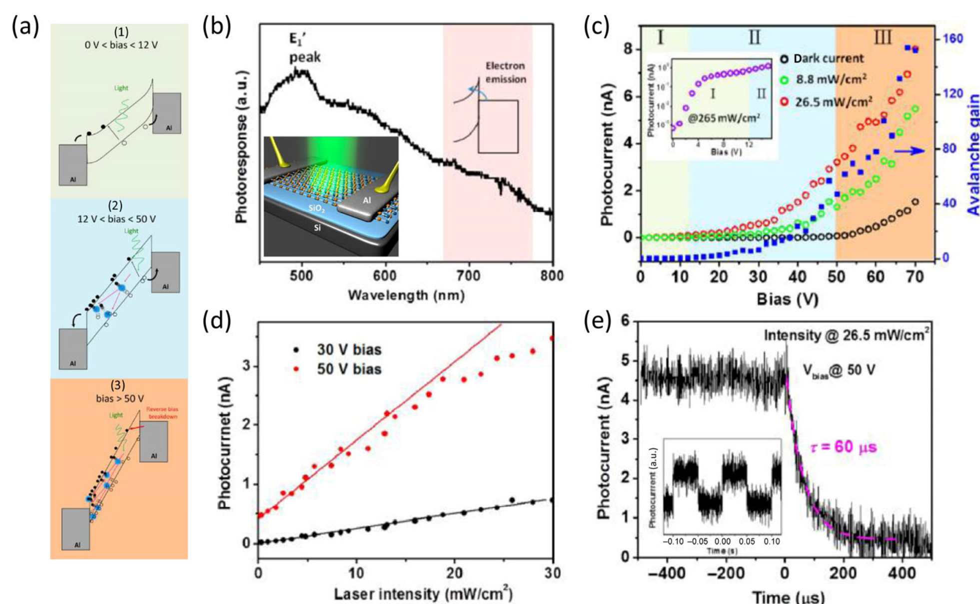

Figure 5 2D InSe avalanche photodetectors. (a) Working mechanisms of 2D InSe avalanche photodetectors under different bias conditions. (i) The bias voltage is between 0 to 12 V. (ii) The bias voltage is between 12 to 50 V. (iii) The bias voltage is greater than 50 V. (b) Device photocurrent response as a function of incident light wavelength. The peak photocurrent response occurs at 510 nm. (c) Device photocurrent and avalanche gain as a function of bias voltage. (d) Device photocurrent as a function of incident laser intensity. (e) Time-resolved photocurrent response showing a decay time of 60 μs. Reproduced with permission from Ref. [76], © American Chemical Society 2015.

5.2 2D BP avalanche photodetectors

Few-layer BP has a direct bandgap of 0.3 eV, which makes 2D BP a promising material candidate for the applications of infrared photodetection [29, 81]. 2D BP-based avalanche photodetectors feature high external quantum efficiency and responsivity at room temperature [77, 78]. Figure 6(a) shows a schematic illustration of a representative BP avalanche photodetector under illumination. M. R. M. Atalla et al. observed that photocurrent increases with increasing bias voltage and the photocurrent spot is initially generated near the positive contact at a low bias voltage and gradually shifts to the negative contact with increasing bias voltage. The shift of photocurrent spot in 2D BP avalanche photodetectors can be explained with the help of band diagram as follows (Fig. 6(b)). During the breakdown process, the holes could tunnel through the Schottky barrier from the contacts and the impact ionization is strong near the positive contact at a small bias, while the large bias voltage could cause tunneling carrier near the negative contact. Therefore, large bias results in large tunneling current near the negative contact, thus photocurrent spot can be observed. Figure 6(c) shows the photocurrent and gain as a function of electric field. The photocurrent of 2D BP avalanche device can be as high as 20 μA at an electric field of 30 kV/cm. In their study, the avalanche gain can be 272 and 7, respectively.

5.3 BP/InSe 2D/2D heterojunction infrared avalanche photodiodes

In 2019, A. Gao et al. observed ballistic avalanche phenomenon in vertically stacked BP and InSe heterostructures [38]. In contrast to conventional avalanche photodetectors with long space charge region, BP/InSe heterojunction has nanoscale active region leading to reduced bias voltage, high gain, and good noise performance, as illustrated in Figs. 7(a) and 7(b). For vertical BP/InSe avalanche photodiode, the channel length

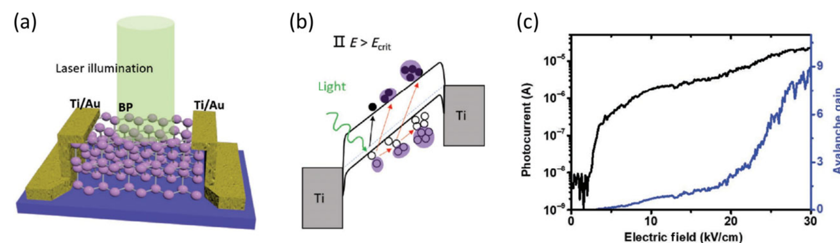

Figure 6 2D BP avalanche photodetectors. (a) Schematic of a 2D BP avalanche photodetector under illumination. (b) Schematic band diagram of 2D BP avalanche photodetectors illustrating the carrier avalanche process. (c) Device photocurrent and avalanche gain as a function of electric field. Reproduced with permission from Ref. [77], © WILEY-VCH Verlag GmbH & Co. KGaA, Weinheim 2019.

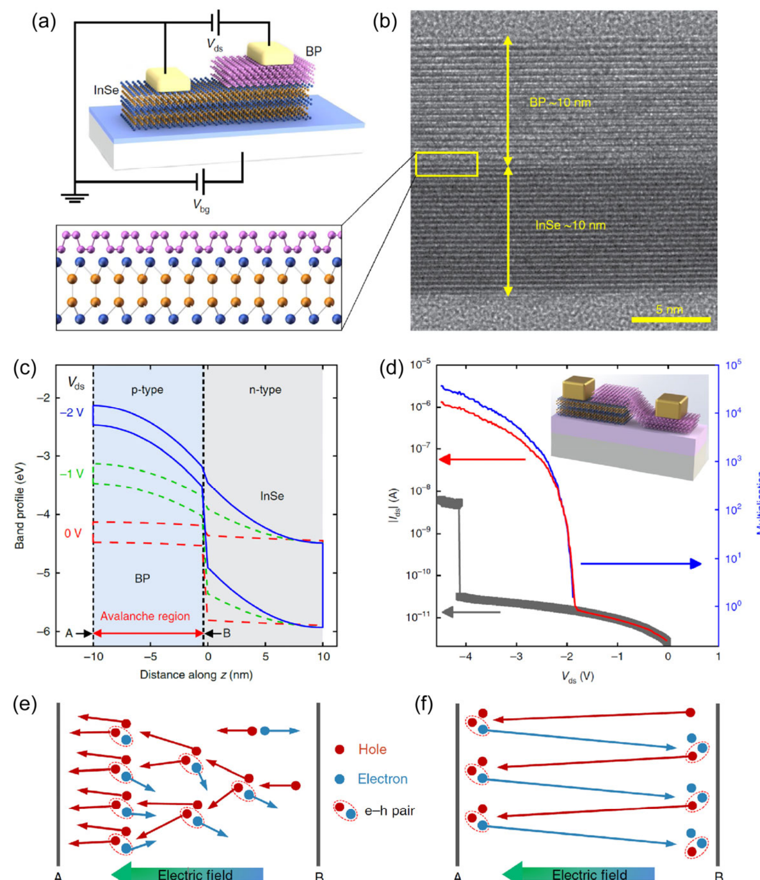

Figure 7 InSe/BP 2D/2D avalanche photodiodes. (a) and (b) Device schematic and transmission electron microscopy (TEM) images of vertically stacked InSe/BP 2D/2D heterojunction avalanche photodiodes. Scale bar, 5 nm. (c) Calculated band diagram of BP/InSe p-n heterojunction under different bias conditions. The impact ionization occurs at 2D BP region. (d) Diode current I_{ds} and multiplication factor as a function of V_{ds}. The device multiplication is over 10^4. (e) Conventional avalanche process under high electric field. (f) Ballistic avalanche process under high electric field. Reproduced with permission from Ref. [38], © Gao, A. Y. et al., under exclusive licence to Springer Nature Limited 2019.

is only 20 nm. Figure 7(c) shows the simulated BP/InSe band profiles with various drain biases ranging from 0 to −2 V at a constant gate bias of 10 V. The band edge of BP is significantly bent even with small drain bias. Therefore, the electric field in the BP region is strong enough to accelerate photo-generated carriers to gain enough energy to initiate impact ionization. Further, the ultraclean van der Waals interfaces enable an exceedingly small hysteresis window in BP/InSe devices. Figure 7(d) shows the photoresponse and multiplication factor as a function of drain bias at a low temperature of 10 K. Under illumination with a wavelength of 4 μm, the BP/InSe devices show abrupt photocurrent response (Fig. 7(d), red line) with an ultrahigh multiplication factor of up to 3×10^4 when the device is biased in the breakdown region at a $V_{ds} = -4.3$ V. More interestingly, the vertical BP/InSe devices exhibit a positive temperature coefficient of avalanche breakdown, which contrasts with conventional avalanche phenomenon. This unique feature is attributed to the ballistic avalanche process, as illustrated in Figs. 7(e) and 7(f) [82]. For example, in conventional avalanche photodiode, impact ionization can generate large amount of randomly distributed charge carriers leading to a large excess noise (Fig. 7(e)). However, for the ballistic avalanche process, the photo-generated hole is accelerated by the electric field and then generates carriers via impact ionization in the region A (Fig. 7(f)). Next, the electrons generated by impact ionization drift to region A and are accelerated by the electric field, and then generate more carriers via impact ionization. The hole generated by electron impact ionization triggers the loop again leading to high multiplication. In 2D BP, the electron and hole have almost the same ionization probabilities because of its symmetric band structure. Therefore, the multiplication process of vertical BP/InSe is attributed to ballistic avalanche.

5.4 MoS_2/silicon 2D/3D heterojunction avalanche photodiodes

2D monolayer TMDs such as MoS_2, WS_2, and WSe_2 etc., could in principle be synthesized in large-scale using chemical vapor deposition (CVD) method [83–85]. Monolayer MoS_2 has a direct bandgap making it interesting for applications in optoelectronics such as light-emitting diodes and photodetectors [86]. More importantly, the material growth and doping technologies of conventional 3D semiconductors, such as silicon, are very mature. The 2D/3D heterostructures could be particularly promising for avalanche photodiode technologies because the monolayer 2D MoS_2 can be used as light absorption layer and the 3D silicon can be used as carrier multiplication layer. Figures 8(a) and 8(b) show the schematic and band diagram of MoS_2/silicon 2D/3D heterojunction avalanche photodiodes [79]. The van der Waals 2D/3D interface can avoid the lattice mismatch issues leading to high-quality p-n junctions [11, 12, 87]. The 2D/3D band structure shows a type-II abrupt hetero-junction. The conduction band offset (E_c) is 200 meV and the valance band offset (E_v) is 900 meV with consideration of their bandgaps and electron affinities. The band offset will be even larger with a reverse bias, which will result in a strong electric field. The strong electric field could accelerate photo-generated carriers and thus initiate avalanche via impact ionization. The MoS_2/silicon 2D/3D avalanche photodiode exhibits a typical p-n diode behavior in the dark condition. Under illumination (wavelength: 633 nm, power: 54.6 nW), the 2D/3D heterojunction p-n diodes show a bias-dependent photocurrent. By using the expression $M = (I_{ph} - I_{dark})/I_{M=1}$, where $I_{M=1}$ is the unity gain photocurrent, the calculated multiplication factor is around 1,500 at a bias voltage of −50 V. The device also shows a high

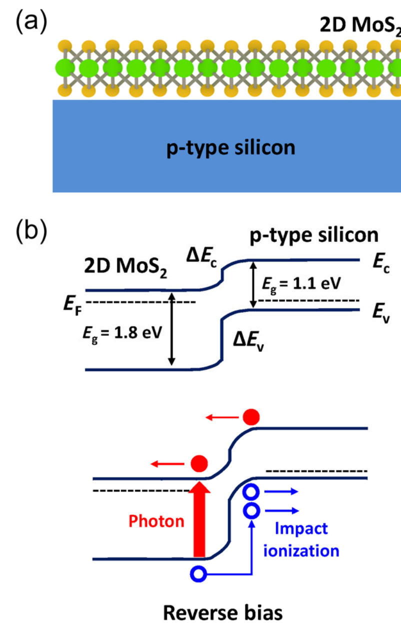

Figure 8 MoS_2/silicon 2D/3D heterojunction avalanche photodiodes. (a) Schematic of a MoS_2/silicon heterojunction avalanche photodetector. (b) Energy band diagram of the MoS_2/silicon heterojunction under equilibrium condition. The incident photon generates an electron–hole pairs, which are accelerated by external electric field. Once the carriers gain sufficient energy, impact ionization occurs, and more electron–hole pairs are generated.

photoresponsivity of 2.2 A/W and a small excess noise factor of around 1.14. So, together with increasing availability of wafer-scale monolayer MoS_2 growth technology, the MoS_2/silicon heterostructures open a new avenue for applications of low-cost and low-noise avalanche photodetectors.

6 Conclusion and outlook

The avalanche photodetectors offer superior performance compared to conventional p-n or p-i-n photodiodes in terms of detection efficiency, photocurrent gain, and response time, so they have been widely used in the field of quantum information technologies such as quantum key distribution [50]. The avalanche photodetectors can be operated above or below the breakdown voltage for different purposes. When the device is operated below breakdown region, the carrier multiplication gain is finite, so they are used for photon energy discrimination and the device output current is propositional to incident photon power. In contrast, when the device is operated above the breakdown region, which is called Geiger mode, the incident photon can trigger avalanche breakdown, leading to significant carrier multiplication, the carrier multiplication is infinite and may trigger a self-sustaining avalanche process, thus enabling single-photon detection [61]. In this review, we have discussed the avalanche phenomenon induced by impact ionization and briefly summarized some recent works on avalanche photodetectors based on 2D materials and their heterostructures. While avalanche photodetectors based on conventional bulk semiconductors have already attained a high level of maturity and are widely used in quantum information technologies for detecting a single photon, in order to meet the demands of new technologies such as light detection and ranging (LiDAR), Time of Flight (ToF), and intelligent robotics etc., a host of emerging 2D material-based photodetectors are being rapidly devised, developed, evaluated, and deployed. The 2D materials provide new strategies for the development of advanced avalanche photodetectors via efficient carrier multiplication at the nanoscale and they may enable a

wide of potential applications in the field of photon-counting technologies.

Acknowledgements

The authors acknowledge the financial support from Washington University in St. Louis and the Institute of Materials Science and Engineering for the use of instruments and staff assistance.

References

[1] Soref, R. A. Silicon-based optoelectronics. *Proc. IEEE* **1993**, *81*, 1687–1706.
[2] Kyomasu, M. Development of an integrated high speed silicon PIN photodiode sensor. *IEEE Trans. Electron. Dev.* **1995**, *42*, 1093–1099.
[3] Li, X. W.; Li, N.; Zheng, X. G.; Demiguel, S.; Campbell, J. C.; Tulchinsky, D. A.; Williams, K. J. High-saturation-current InP-InGaAs photodiode with partially depleted absorber. *IEEE Photonics Technol. Lett.* **2003**, *15*, 1276–1278.
[4] Murakami, H.; Akiba, M.; Matsumoto, T.; Noda, M. Low-noise infrared detection system with InSb photodiode for infrared astronomy. *Jpn. J. Appl. Phys.* **1988**, *27*, L1973–L1975.
[5] Reine, M. B. HgCdTe photodiodes for IR detection: A review. In *Proceedings of SPIE 4288, Photodetectors: Materials and Devices VI*, San Jose, USA, 2001, pp 266–277.
[6] Akinwande, D.; Huyghebaert, C.; Wang, C. H.; Serna, M. I.; Goossens, S.; Li, L. J.; Wong, H. S. P.; Koppens, F. H. L. Graphene and two-dimensional materials for silicon technology. *Nature* **2019**, *573*, 507–518.
[7] Lan, C. Y.; Zhou, Z. Y.; Zhou, Z. F.; Li, C.; Shu, L.; Shen, L. F.; Li, D. P.; Dong, R. T.; Yip, S. P.; Ho, J. C. Wafer-scale synthesis of monolayer WS_2 for high-performance flexible photodetectors by enhanced chemical vapor deposition. *Nano Res.* **2018**, *11*, 3371–3384.
[8] Bonaccorso, F.; Sun, Z.; Hasan, T.; Ferrari, A. C. Graphene photonics and optoelectronics. *Nat. Photonics* **2010**, *4*, 611–622.
[9] Xia, F. N.; Wang, H.; Xiao, D.; Dubey, M.; Ramasubramaniam, A. Two-dimensional material nanophotonics. *Nat. Photon.* **2014**, *8*, 899–907.
[10] Miao, J. S.; Zhang, L.; Wang, C. Black phosphorus electronic and optoelectronic devices. *2D Mater.* **2019**, *6*, 032003.
[11] Jariwala, D.; Marks, T. J.; Hersam, M. C. Mixed-dimensional van der Waals heterostructures. *Nat. Mater.* **2017**, *16*, 170–181.
[12] Liu, Y.; Huang, Y.; Duan, X. F. van der Waals integration before and beyond two-dimensional materials. *Nature* **2019**, *567*, 323–333.
[13] Gan, X. T.; Shiue, R. J.; Gao, Y. D.; Meric, I.; Heinz, T. F.; Shepard, K.; Hone, J.; Assefa, S.; Englund, D. Chip-integrated ultrafast graphene photodetector with high responsivity. *Nat. Photonics* **2013**, *7*, 883–887.
[14] Pospischil, A.; Humer, M.; Furchi, M. M.; Bachmann, D.; Guider, R.; Fromherz, T.; Mueller, T. CMOS-compatible graphene photodetector covering all optical communication bands. *Nat. Photonics* **2013**, *7*, 892–896.
[15] Mueller, T.; Xia, F. N.; Avouris, P. Graphene photodetectors for high-speed optical communications. *Nat. Photonics* **2010**, *4*, 297–301.
[16] Liu, C. H.; Chang, Y. C.; Norris, T. B.; Zhong, Z. H. Graphene photodetectors with ultra-broadband and high responsivity at room temperature. *Nat. Nanotechnol.* **2014**, *9*, 273–278.
[17] Furchi, M.; Urich, A.; Pospischil, A.; Lilley, G.; Unterrainer, K.; Detz, H.; Klang, P.; Andrews, A. M.; Schrenk, W.; Strasser, G. et al. Microcavity-integrated graphene photodetector. *Nano Lett.* **2012**, *12*, 2773–2777.
[18] Xia, F. N.; Mueller, T.; Lin, Y. M.; Valdes-Garcia, A.; Avouris, P. Ultrafast graphene photodetector. *Nat. Nanotechnol.* **2009**, *4*, 839–843.
[19] Miao, J. S.; Hu, W. D.; Guo, N.; Lu, Z. Y.; Liu, X. Q.; Liao, L.; Chen, P. P.; Jiang, T.; Wu, S. W.; Ho, J. C. et al. High-responsivity graphene/InAs nanowire heterojunction near-infrared photodetectors with distinct photocurrent on/off ratios. *Small* **2015**, *11*, 936–942.
[20] Yin, Z. Y.; Li, H.; Li, H.; Jiang, L.; Shi, Y. M.; Sun, Y. H.; Lu, G.; Zhang, Q.; Chen, X. D.; Zhang, H. Single-layer MoS_2 phototransistors. *ACS Nano* **2012**, *6*, 74–80.
[21] Wang, X. D.; Wang, P.; Wang, J. L.; Hu, W. D.; Zhou, X. H.; Guo, N.; Huang, H.; Sun, S.; Shen, H.; Lin, T. et al. Ultrasensitive and broadband MoS_2 photodetector driven by ferroelectrics. *Adv. Mater.* **2015**, *27*, 6575–6581.
[22] Lee, C. H.; Lee, G. H.; Van Der Zande, A. M.; Chen, W. C.; Li, Y. L.; Han, M. Y. Cui, X.; Arefe, G.; Nuckolls, C. et al. Atomically thin p-n junctions with van der Waals heterointerfaces. *Nat. Nanotechnol.* **2014**, *9*, 676–681.
[23] Li, L. K.; Yu, Y. J.; Ye, G. J.; Ge, Q. Q.; Ou, X. D.; Wu, H.; Feng, D. L.; Chen, X. H.; Zhang, Y. B. Black phosphorus field-effect transistors. *Nat. Nanotechnol.* 2014, ***9***, 372–377.
[24] Viti, L.; Hu, J.; Coquillat, D.; Knap, W.; Tredicucci, A.; Politano, A.; Vitiello, M. S. Black phosphorus terahertz photodetectors. *Adv. Mater.* **2015**, *27*, 5567–5572.
[25] Deng, Y. X.; Luo, Z.; Conrad, N. J.; Liu, H.; Gong, Y. J.; Najmaei, S.; Ajayan, P. M.; Lou, J.; Xu, X. F.; Ye, P. D. Black phosphorus-monolayer MoS_2 van der Waals heterojunction p-n diode. *ACS Nano* **2014**, *8*, 8292–8299.
[26] Huang, M. Q.; Wang, M. L.; Chen, C.; Ma, Z. W.; Li, X. F.; Han, J. B.; Wu, Y. Q. Broadband black-phosphorus photodetectors with high responsivity. *Adv. Mater.* **2016**, *28*, 3481–3485.
[27] Yuan, H. T.; Liu, X. G.; Afshinmanesh, F.; Li, W.; Xu, G.; Sun, J.; Lian, B.; Curto, A. G.; Ye, G. J.; Hikita, Y. et al. Polarization-sensitive broadband photodetector using a black phosphorus vertical p-n junction. *Nat. Nanotechnol.* **2015**, *10*, 707–713.
[28] Youngblood, N.; Chen, C.; Koester, S. J.; Li M. Waveguide-integrated black phosphorus photodetector with high responsivity and low dark current. *Nat. Photonics* **2015**, *9*, 247–252.
[29] Chen, X. L.; Lu, X. B.; Deng, B. C.; Sinai, O.; Shao, Y. C.; Li, C.; Yuan, S. F.; Tran, V.; Watanabe, K.; Taniguchi, T. et al. Widely tunable black phosphorus mid-infrared photodetector. *Nat. Commun.* 2017, ***8***, 1672.
[30] Buscema, M.; Groenendijk, D. J.; Blanter, S. I.; Steele, G. A.; Van Der Zant, H. S. J.; Castellanos-Gomez, A. Fast and broadband photoresponse of few-layer black phosphorus field-effect transistors. *Nano Lett.* **2014**, *14*, 3347–3352.
[31] Jariwala, D.; Sangwan, V. K.; Wu, C. C.; Prabhumirashi, P. L.; Geier, M. L.; Marks, T. J.; Lauhon, L. J.; Hersam, M. C. Gate-tunable carbon nanotube-MoS_2 heterojunction p-n diode. *Proc. Natl. Acad. Sci. USA* **2013**, *110*, 18076–18080.
[32] Li, X. M.; Zhu, H. W.; Wang, K. L.; Cao, A. Y.; Wei, J. Q.; Li, C. Y.; Jia, Y.; Li, Z.; Li. X.; Wu, D. H. Graphene-on-silicon Schottky junction solar cells. *Adv. Mater.* **2010**, *22*, 2743–2748.
[33] Bullock, J.; Amani, M.; Cho, J.; Chen, Y. Z.; Ahn, G. H.; Adinolfi, V.; Shrestha, V. R.; Gao, Y.; Crozier, K. B.; Chueh, Y. L. et al. Polarization-resolved black phosphorus/molybdenum disulfide mid-wave infrared photodiodes with high detectivity at room temperature. *Nat. Photonics* **2018**, *12*, 601–607.
[34] Wang, P.; Liu, S. S.; Luo, W. J.; Fang, H. H.; Gong, F.; Guo, N.; Chen, Z. G.; Zou, J.; Huang, Y.; Zhou, X. H. et al. Arrayed van Der waals broadband detectors for dual-band detection. *Adv. Mater.* **2017**, *29*, 1604439.
[35] Kufer, D.; Nikitskiy, I.; Lasanta, T.; Navickaite, G.; Koppens, F. H. L.; Konstantatos G. Hybrid 2D-0D MoS_2-PbS quantum dot photodetectors. *Adv. Mater.* **2015**, *27*, 176–180.
[36] Choi, W.; Cho, M. Y.; Konar, A.; Lee, J. H.; Cha, G. B.; Hong, S. C.; Kim, S.; Kim, J.; Jena, D.; Joo, J. et al. High-detectivity multilayer MoS_2 phototransistors with spectral response from ultraviolet to infrared. *Adv. Mater.* **2012**, *24*, 5832–5836.
[37] Cai, X. H.; Sushkov, A. B.; Suess, R. J.; Jadidi, M. M.; Jenkins, G. S.; Nyakiti, L. O.; Myers-Ward, R. L.; Li, S. S.; Yan, J.; Gaskill, D. K. et al. Sensitive room-temperature terahertz detection via the photo-thermoelectric effect in graphene. *Nat. Nanotechnol.* **2014**, *9*, 814–819.
[38] Gao, A. Y.; Lai, J. W.; Wang, Y. J.; Zhu, Z.; Zeng, J. W.; Yu, G. L.; Wang, N. Z.; Chen, W. C.; Cao, T. J.; Hu, W. D. et al. Observation of ballistic avalanche phenomena in nanoscale vertical InSe/BP heterostructures. *Nat. Nanotechnol.* **2019**, *14*, 217–222.
[39] Guo, Q. S.; Pospischil, A.; Bhuiyan, M.; Jiang, H.; Tian, H.; Farmer, D.; Deng, B. C.; Li, C.; Han, S. J.; Wang, H. et al. Black phosphorus mid-infrared photodetectors with high gain. *Nano Lett.* **2016**, *16*, 4648–4655.

[40] Buscema, M.; Barkelid, M.; Zwiller, V.; van der Zant, H. S.; Steele, G. A.; Castellanos-Gomez, A. Large and tunable photothermoelectric effect in single-layer MoS_2. *Nano Lett*. **2013**, *13*, 358–363.

[41] Miao, J. S.; Song, B.; Li, Q.; Cai, L.; Zhang, S. M.; Hu, W. D.; Dong, L. X.; Wang, C. Photothermal effect induced negative photoconductivity and high responsivity in flexible black phosphorus transistors. *ACS Nano* **2017**, *11*, 6048–6056.

[42] Furchi, M. M.; Pospischil, A.; Libisch, F.; Burgdörfer, J.; Mueller T. Photovoltaic effect in an electrically tunable van der Waals heterojunction. *Nano Lett*. **2014**, *14*, 4785–4791.

[43] Lopez-Sanchez, O.; Lembke, D.; Kayci, M.; Radenovic, A.; Kis, A. Ultrasensitive photodetectors based on monolayer MoS_2. *Nat. Nanotechnol*. **2013**, *8*, 497–501.

[44] Freitag, M.; Low, T.; Xia, F. N.; Avouris, P. Photoconductivity of biased graphene. *Nat. Photonics* **2013**, *7*, 53–59.

[45] Furchi, M. M.; Polyushkin, D. K.; Pospischil, A.; Mueller T. Mechanisms of photoconductivity in atomically thin MoS_2. *Nano Lett*. **2014**, *14*, 6165–6170.

[46] Li, T. L.; Hsu, S. L. C. Enhanced thermal conductivity of polyimide films via a hybrid of micro-and nano-sized boron nitride. *J. Phys. Chem. B* **2010**, *114*, 6825–6829.

[47] Glassbrenner, C. J.; Slack, G. A. Thermal conductivity of silicon and germanium from 3 K to the melting point. *Phys. Rev*. **1964**, *134*, A1058–A1069.

[48] Cova, S.; Ghioni, M.; Lacaita, A.; Samori, C.; Zappa, F. Avalanche photodiodes and quenching circuits for single-photon detection. *Appl. Opt*. **1996**, *35*, 1956–1976.

[49] Dautet, H.; Deschamps, P.; Dion, B.; MacGregor, A. D.; MacSween, D.; McIntyre, R. J.; Trottier, C.; Webb, P. P. Photon counting techniques with silicon avalanche photodiodes. *Appl. Opt.* **1993**, *32*, 3894–3900.

[50] Hadfield, R. H. Single-photon detectors for optical quantum information applications. *Nat. Photonics* **2009**, *3*, 696–705.

[51] Stillman, G. E.; Wolfe, C. M. Avalanche photodiodes. In *Semiconductors and Semimetals*; Willardson, R. K.; Beer, A. C., Eds.; Elsevier: Amsterdam, 1977; pp 291–393.

[52] Diepold, M.; Fernandes, L. M. P.; Machado, J.; Amaro, P.; Abdou-Ahmed, M.; Amaro, F. D.; Antognini, A.; Biraben, F.; Chen, T. L.; Covita, D. S. et al. Improved X-ray detection and particle identification with avalanche photodiodes. *Rev. Sci. Instrum*. **2015**, *86*, 053102.

[53] Kasap, S. O. *Optoelectronics and Photonics*: *Principles and Practices*; Pearson: Prentice Hall, 2001.

[54] Ghioni, M.; Gulinatti, A.; Rech, I.; Zappa, F.; Cova, S. Progress in silicon single-photon avalanche diodes. *IEEE J. Sel. Topics Quantum Electron*. **2007**, *13*, 852–862.

[55] Zhang, J.; Itzler, M. A.; Zbinden, H.; Pan, J. W. Advances in InGaAs/InP single-photon detector systems for quantum communication. *Light Sci. Appl*. **2015**, *4*, e286.

[56] Namekata, N.; Sasamori, S.; Inoue, S. 800 MHz single-photon detection at 1550-nm using an InGaAs/InP avalanche photodiode operated with a sine wave gating. *Opt. Express* **2006**, *14*, 10043–10049.

[57] Ando, H.; Kanbe, H.; Kimura, T.; Yamaoka, T.; Kaneda, T. Characteristics of germanium avalanche photodiodes in the wavelength region of 1–1.6 µm. *IEEE J. Quantum Electron*. **1978**, *14*, 804–809.

[58] Duraffourg, L.; Merolla, J. M.; Goedgebuer, J. P.; Butterlin, N.; Rhodes, W. T. Photon counting in the 1540-nm wavelength region with a germanium avalanche photodiode. *IEEE J. Quantum Electron*. **2001**, *37*, 75–79.

[59] Assefa, S.; Xia, F. N.; Vlasov, Y. A. Reinventing germanium avalanche photodetector for nanophotonic on-chip optical interconnects. *Nature* **2010**, *464*, 80–84.

[60] Tosi, A.; Calandri, N.; Sanzaro, M.; Acerbi, F. Low-noise, low-jitter, high detection efficiency InGaAs/InP single-photon avalanche diode. *IEEE J. Sel. Topics Quantum Electron*. **2014**, *20*, 3803406.

[61] Renker, D. Geiger-mode avalanche photodiodes, history, properties and problems. *Nucl. Instrum. Methods Phys. Res. Sect. A* **2006**, *567*, 48–56.

[62] Hall, D.; Liu, Y. H.; Lo, Y. H. Single photon avalanche detectors: Prospects of new quenching and gain mechanisms. *Nanophotonics* **2015**, *4*, 397–412.

[63] Goetzberger, A.; McDonald, B.; Haitz, R. H.; Scarlett, R. M. Avalanche effects in silicon p-n junctions. II. Structurally perfect junctions. *J. Appl. Phys*. **1963**, *34*, 1591–1600.

[64] Haitz, R. H. Mechanisms contributing to the noise pulse rate of avalanche diodes. *J. Appl. Phys*. **1965**, *36*, 3123–3131.

[65] Zang, K.; Jiang, X.; Huo, Y. J.; Ding, X.; Morea, M.; Chen, X. C.; Lu, C. Y.; Ma, J.; Zhou, M.; Xia, Z. Y. et al. Silicon single-photon avalanche diodes with nano-structured light trapping. *Nat. Commun*. **2017**, *8*, 628.

[66] Kang, Y. M.; Liu, H. D.; Morse, M.; Paniccia, M. J.; Zadka, M.; Litski, S.; Zadka, M.; Litski, S.; Sarid, G.; Pauchard, A. et al. Monolithic germanium/silicon avalanche photodiodes with 340 GHz gain-bandwidth product. *Nat. Photonics* **2009**, *3*, 59–63.

[67] Susa, N.; Nakagome, H.; Mikami, O.; Ando, H.; Kanbe, H. New InGaAs/InP avalanche photodiode structure for the 1–1.6 µm wavelength region. *IEEE J. Quantum Electron*. **1980**, *16*, 864–870.

[68] Tosi, A.; Acerbi, F.; Anti, M.; Zappa, F. InGaAs/InP single-photon avalanche diode with reduced afterpulsing and sharp timing response with 30 ps tail. *IEEE J. Quantum Electron*. **2012**, *48*, 1227–1232.

[69] Itzler, M. A.; Ben-Michael, R.; Hsu, C. F.; Slomkowski, K.; Tosi, A.; Cova, S.; Zappa, F.; Ispasoiu, R. Single photon avalanche diodes (SPADs) for 1.5 µm photon counting applications. *J. Mod. Opt*. **2007**, *54*, 283–304.

[70] Hayden, O.; Agarwal, R.; Lieber, C. M. Nanoscale avalanche photodiodes for highly sensitive and spatially resolved photon detection. *Nat. Mater*. **2006**, *5*, 352–356.

[71] Bulgarini, G.; Reimer, M. E.; Hocevar, M.; Bakkers, E. P. A. M.; Kouwenhoven, L. P.; Zwiller, V. Avalanche amplification of a single exciton in a semiconductor nanowire. *Nat. Photonics* **2012**, *6*, 455–458.

[72] Farrell, A. C.; Meng, X.; Ren, D. K.; Kim, H.; Senanayake, P.; Hsieh, N. Y.; Rong, Z. X.; Chang, T. Y.; Azizur-Rahman, K. M.; Huffaker, D. L. InGaAs-GaAs nanowire avalanche photodiodes toward single-photon detection in free-running mode. *Nano Lett*. **2019**, *19*, 582–590.

[73] Gibson, S. J.; van Kasteren, B.; Tekcan, B.; Cui, Y. C.; van Dam, D.; Haverkort, J. E. M.; Bakkers, E. P. A. M.; Reimer, M. E.. Tapered InP nanowire arrays for efficient broadband high-speed single-photon detection. *Nat. Nanotechnol*. **2019**, *14*, 473–479.

[74] Huang, L.; Dong, B. W.; Guo, X.; Chang, Y. H.; Chen, N.; Huang, X.; Liao, W. G.; Zhu, C. X.; Wang, H.; Lee, C. et al. Waveguide-integrated black phosphorus photodetector for mid-infrared applications. *ACS Nano* **2019**, *13*, 913–921.

[75] Song, S. C.; Chen, Q.; Jin, L.; Sun, F. H. Great light absorption enhancement in a graphene photodetector integrated with a metamaterial perfect absorber. *Nanoscale* **2013**, *5*, 9615–9619.

[76] Lei, S. D.; Wen, F. F.; Ge, L. H.; Najmaei, S.; George, A.; Gong, Y. J.; Gao, W. L.; Jin, Z. H.; Li. B.; Lou, J. et al. An atomically layered InSe avalanche photodetector. *Nano Lett*. **2015**, *15*, 3048–3055.

[77] Jia, J. Y.; Jeon, J.; Park, J. H.; Lee, B. H.; Hwang, E.; Lee S. Avalanche carrier multiplication in multilayer black phosphorus and avalanche photodetector. *Small* **2019**, *15*, 1805352.

[78] Atalla, M. R. M.; Koester, S. J. Black phosphorus avalanche photodetector. In *Proceedings of the 75th Annual Device Research Conference* (*DRC*), South Bend, USA, 2017, pp 1–2.

[79] Lopez-Sanchez, O.; Dumcenco, D.; Charbon, E.; Kis, A. Avalanche photodiodes based on MoS_2/Si heterojunctions. 2014, arXiv: 1411.3232. arXiv.org e-Print archive. https://arxiv.org/abs/1411.3232 (accessed Nov 12, 2014).

[80] Dai, M. J.; Chen, H. Y.; Feng, R.; Feng, W.; Hu, Y. X.; Yang, H. H.; Liu, G. B.; Chen, X. S.; Zhang, J.; Xu, C. Y. et al. A dual-band multilayer InSe self-powered photodetector with high performance induced by surface plasmon resonance and asymmetric Schottky junction. *ACS Nano* **2018**, *12*, 8739–8747.

[81] Engel, M.; Steiner, M.; Avouris, P. Black phosphorus photodetector for multispectral, high-resolution imaging. *Nano Lett*. **2014**, *14*, 6414–6417.

[82] Hollenhorst, J. N. Ballistic avalanche photodiodes: Ultralow noise avalanche diodes with nearly equal ionization probabilities. *Appl. Phys. Lett*. **1986**, *49*, 516–518.

[83] Kang, K.; Lee, K. H.; Han, Y. M.; Gao, H.; Xie, S. E.; Muller, D. A.; Park, J. Layer-by-layer assembly of two-dimensional materials into wafer-scale heterostructures. *Nature* **2017**, *550*, 229–233.

[84] Chen, J. J.; Shao, K.; Yang, W. H.; Tang, W. Q.; Zhou, J. P.; He, Q. M.; Wu, Y. P.; Zhang, C. M.; Li, X.; Yang, X. et al. Synthesis of wafer-scale monolayer WS_2 crystals toward the application in integrated electronic devices. *ACS Appl*. *Mater*. *Interfaces* **2019**, *11*, 19381–19387.

[85] Cun, H. Y.; Macha, M.; Kim, H. K.; Liu, K.; Zhao, Y. F.; LaGrange, T.; Kis, S.; Radenovic, A. Wafer-scale MOCVD growth of monolayer MoS_2 on sapphire and SiO_2. *Nano Res*. **2019**, *12*, 2646–2652.

[86] Salehzadeh, O.; Tran, N. H.; Liu, X.; Shih, I.; Mi, Z. Exciton kinetics, quantum efficiency, and efficiency droop of monolayer MoS_2 light-emitting devices. *Nano Lett*. **2014**, *14*, 4125–4130.

[87] Miao, J. S.; Liu, X. W.; Jo, K.; He, K.; Saxena, R.; Song, B. K.; Zhang, H. Q.; He, J. L.; Han, M. G.; Hu, W. D. et al. Gate-tunable semiconductor heterojunctions from 2D/3D van der waals interfaces. *Nano Lett*. **2020**, *20*, 2907–2915.